PCCP

Accepted Manuscript

ROYAL SOCIETY OF CHEMISTRY

www.rsc.org/pccp

CO Oxidation Catalyzed by Pt-embedded Graphene: A First-principles Investigation

Xin Liu†,* *Yanhui Sui*†, *Ting Duan*†, *Changong Meng*†, *Yu Han*‡

† School of Chemistry, Dalian University of Technology, Dalian, 116024, P. R. China

‡ Advanced Membranes and Porous Materials Center, King Abdullah University of Science and Technology, Thuwal, 23955-6900, Kingdom of Saudi Arabia

*Corresponding Author:

Dr. Xin Liu

Tel: +86-411-84986343

Email: xliu@dlut.edu.cn

ABSTRACT

We addressed the potential catalytic role of Pt-embedded graphene in CO oxidation by first-principles-based calculations. We showed that the combination of highly reactive Pt atoms and defects over graphene makes the Pt-embedded graphene a superior mono-dispersed atomic catalyst for CO oxidation. The binding of a single Pt atom onto monovacancy defects is up to -7.10 eV, which not only ensure the high stability of the embedding, but also vigorously excludes the possibility for diffusion and aggregation of embedded Pt atoms. This strong interfacial interaction also tunes the energy level of Pt-d states for the activation of O_2, and promotes the formation and dissociation of the peroxide-like intermediate. The catalytic cycle of CO oxidation is initiated through the Langmuir–Hinshelwood mechanism, with the formation of a peroxide-like intermediate by the coadsorbed CO and O_2, by the dissociation of which the a CO_2 molecule and an adsorbed O atom are formed. Then, another gaseous CO will react with the remnant O atom and make the embedded Pt atom as available for the subsequent reaction. The calculated energy barriers for the formation and dissociation of peroxide-like intermediate are as low as 0.33 and 0.15 eV, respectively, while that for the regeneration of the embedded Pt atom is 0.46 eV, indicating the potential high catalytic performance of Pt-embedded graphene for low temperature CO oxidation.

KEYWORDS: Graphene; single vacancy graphene; defects; Pt; CO; oxidation;

1. INTRODUCTION

The low-temperature oxidation of carbon monoxide (CO) plays an important role in solving the growing environmental problems caused by CO emission. Supported transition metal (TM) nanoparticles (NPs) are commonly used catalysts for CO oxidation. Though TMs such as Pt, Pd, Ru and etc. can effectively catalyze the CO oxidation , the reaction kinetics would be sluggish at low temperatures because CO occupies the surface sites, leaving no sites for adsorption and activation of oxygen. [1-6] Considerable efforts have been made to develop novel and efficient catalysts for low temperature CO oxidation.[7-11]

Recently, supported subnanometer-sized TM NPs or even single TM atom are found to exhibit superior catalytic activity and selectivity than conventional nano-sized particles in a large number of important chemical reactions, including CO oxidation.[7-10, 12-14] For example, Zhang *et al.* reported the fabrication of a Pt single-atom catalyst by anchoring isolated Pt atoms onto surface defect of iron oxide NPs, which exhibits exceptional high activity and stability for CO oxidation. They also realized the high activity and selectivity of monodispersed Ir atom over iron hydroxide NPs in preferential oxidation of CO in a H_2-rich gas.[8, 9] Xu et al observed the superior catalytic performance of Au atoms embedded onto nanosized ZrO_2 support in 1,3-butadiene and they showed that the improved catalytic performance is due to the embedded charged Au atoms.[15] The underlying enhancing mechanisms are not always straightforward. Unlike NPs of sp metals, where the impact of quantum size effect would be significant due to free-electron like behavior of s and p electrons,[16] the reactivity of TM NPs are determined by their localized d states.[17] Therefore, low-coordination and unsaturated atoms often function as reaction sites over TM NPs [18] and downsizing the particles to single atoms is highly desirable to maintain a high density of active sites for catalytic reactions.[19]

On the other hand, the support–metal interaction in deposited TM NPs is also of great importance. This interaction would raise strains, shift the energy levels, redistribute electron density of the NP states and thus change the catalytic activity of the nanocatalysts. For example, Oh *et al.* investigated CO adsorption on Fe and Pt NPs deposited on graphenic carbon and they attributed the weakening of the CO-TM interaction to the formation of TM-carbon contact.[20, 21] Similarly, small Pt NPs deposited on graphenic support have been proved to be CO tolerant when used as the electrode material for fuel cells.[22] Careful selection of the support allows the electronic states in the TM NPs to be finely tuned, making the TM NPs highly reactive or completely inert.[23-28] This interfacial interaction may also help to effectively stabilize the monodispersed TM NPs or atoms and prohibit them from sintering under realistic reaction conditions, which are one of the key challenges for fabrication of practical and stable single-atom catalysts.[29] To this end, a careful screening of the metal-support interactions would be necessary for the rational design of monodispersed ultrafine TM NPs or single TM atoms as efficient catalyst for a specific reaction.

Many studies on supported metal NPs show that surface defects of the supports could serve as anchoring sites for metal clusters or even single atoms. Various defects, including boundaries, dopants, vacancies and etc in graphene have also been proposed to modulate the electronic structures and so as the catalytic performance of supported TM NPs and atoms.[30-35] Recently, heteroatom-embedded graphene was fabricated under electron-beam radiation,[36] and Au, Cu, and Fe embedded graphene have been proposed to be efficient for CO oxidation by theoretical calculations. The promoted catalytic activity can be attributed to the partially occupied d states localized in the vicinity of the Fermi level due to the interaction of the TM atom with graphene. [37-40] These experimental and theoretical investigations provide strong evidence that fabrication of

mono-dispersed TM atom catalyst by introduction of defects onto the support is feasible and the resulting catalyst can display unusual behaviors compared with conventional catalysts.

Inspired by these work, we investigated the electronic structure and potential catalytic role of Pt-embedded graphene in CO oxidation by first-principles-based calculations. We showed that the combination of highly reactive Pt atoms and defects over graphene makes the Pt-embedded graphene a superior mono-dispersed atomic catalyst for CO oxidation. The strong binding of a single Pt atom onto monovacancy graphene will not only ensure the high stability of the embedding, but also vigorously excludes the possibility for embedded Pt atoms to aggregate. This interfacial interaction also tunes the energy level of Pt-d states for the activation of O_2, and promotes the formation and dissociation of the peroxide-like intermediate. The CO oxidation over Pt-embedded graphene would proceed through the Langmuir–Hinshelwood mechanism. The calculated energy barriers for the formation and dissociation of peroxide-like intermediate are as low as 0.33 and 0.15 eV, respectively, while that for the regeneration of the embedded Pt atom is 0.46 eV, indicating the potential high catalytic performance of Pt-embedded graphene for low temperature CO oxidation. These findings pave the way for the developments of effective CO oxidation catalysts with high stability and superior catalytic performance. The rest of the paper is organized as the following: the theoretical methods and computational details are described in Section 2, the results are presented and discussed in Section 3 and concluded in Section 4.

2. THEORETICAL METHODS

The first-principles based calculations were carried out using the DMol^3 package.[41, 42] Perdew-Burke-Ernzerhof (PBE) functional within the formulation of gradient approximation (GGA) was used to handle the exchange and correlations.[43] The ion-electron interaction is described with

DFT semicore pseudopotentials (DSPPs) and a double numerical basis set including a d-polarization function (DND).[44] Within this scheme, the C and O atoms were treated with all-electron basis sets, while the core Pt electrons were treated by DSPP pseudopotential and the valence Pt electrons were treated with DND basis sets. To lower the computational cost in geometry optimization, the substrate and the embedded composites were preoptimized with empirical potential,[45, 46] and then were fully relaxed within the aforementioned ab-initio scheme until the residue forces were reduced below 1×10^{-2} eV/Å. To ensure high-quality results, the real-space global orbital cutoff radius was chosen as 4.6 Å. All self-consistent field (SCF) calculations were performed with a convergence criterion of 2×10^{-4} eV on the total energy. With the above setup, the bulk lattice parameter of face-center-cubic Pt is reproduced as a =3.98 Å, while the minimum C-C distance in pristine graphene is 1.42 Å.[47, 48]

A hexagonal 4 × 4 supercell of pristine graphene was used to mimic the graphene and the Pt embedded graphene. Embedding of Pt atom was done by substituting one C atom with a Pt atom. The minimum distance between the graphene sheet and its mirror images is set to be larger than 20 Å to avoid the interactions among them. Brillouin zone integration was sampled over a Γ centered 4 × 4 × 1 *k*-point grid in geometric optimization and the search for the transition state (TS), while a 20 × 20 × 1 Monkhorst-Pack *k*-point grid was used to explore the electronic structures.[49] Test calculations using a 162-atom supercell gave essentially the same results. The amount of charge transfer was investigated within the Hirshfeld scheme.[50]

The transition states were located through the synchronous method with conjugated gradient refinements.[51] This method involves linear synchronous transit (LST) maximization, followed by repeated conjugated gradient (CG) minimizations, and then quadratic synchronous transit (QST) maximizations and repeated CG minimizations until a transition state is located.

The formation energy of defect in graphene (E_f) is calculated as $E_f = E_d - \frac{m}{n} E_p$, where E_d and E_p are the total energies of defective and pristine graphene, respectively, n is the number of atoms in the pristine graphene, while m is the number of atoms in the defective graphene.

The binding energy (E_b) of Pt atom onto graphene(GN) is calculated as the energy difference between the Pt atomically deposited graphene (PtGN) and the separated graphene plus the freestanding Pt atom, following Equation (1).

$$E_b = E_{PtGN} - (E_{Pt} + E_{GN}) \quad (1)$$

For the study concerning adsorption of CO, O_2, O and etc., the adsorption energy (E_{ad}) is calculated as the energy difference between the species absorbed Pt deposited graphene and the gaseous species plus the bare PtGN, following Equation (2).

$$E_{ad} = E_{adsorbate+PtGN} - (E_{PtGN} + E_{adsorbate}) \quad (2)$$

3. RESULTS AND DISCUSSIONS

3.1 Pt atomic deposition on graphene

The optimized structures, binding energies for the Pt atoms deposited on pristine graphene (PG) and embedded in defective graphene (MG) are summarized in Table 1. According to the symmetry of graphene lattice, there are 3 possible deposition structures, namely, the Atop site that is on top of a C atom, the Brg site that is in the middle of 2 adjacent C atoms and the Hol site that is on top of the center of a C_6 ring.

Table 1. Optimized structures and energetics for Pt atomic deposition on graphene.

Model		E_b[a] (eV)	h[b] (Å)	Min R_{Pt-C}[c] (Å)	Δq[d] (e)
Pristine graphene					
	Atop	-1.89	2.04	2.04	0.03
	Brg	-2.03	1.98	2.10	0.09
	Hol	-1.41	1.97	2.43	0.01
Monovacancy graphene					
	PtMG	-7.10	1.76	1.94	0.51

[a] The binding energy of Pt atom onto PG and MG, calculated from Equation 1.
[b] The distance of Pt atom from the basal plane of graphene.
[c] The minimum distance from the deposited Pt atom to C atom on graphene.
[d] The amount of charge transfer from Pt atom to the graphene.

The most plausible structure for Pt atomic deposition over PG is at Brg and the calculated E_b is -2.03 eV. In this configuration, Pt atom stands right above 2 neighboring C atoms and the nearest Pt-C distance is 2.10 Å, which falls into the range of typical Pt-C chemical bonds observed in various Pt based complexes.[52] This chemical interaction is contributed by the C-p states and the in-plane components Pt-d states. To match the interaction with Pt atom, the surrounding C atoms will move out of the basal plane of graphene lattice. Depending on the size of cell used, the magnitude of this corrugation various in the range from 0.28 to 0.35 Å. The E_b at Atop and Hol are unfavored by 0.14 and 0.62 eV as compared with that at Brg, respectively. As for the Atop configuration, the Pt atom stands 2.04 Å above a C atom. As a single C-sp state is not enough to stabilize the Pt-d and Pt-sp states, the calculated E_b is only -1.89 eV. In the Hol configuration, the Pt atom lies 1.97 Å above the center of a C_6 ring and the nearest Pt-C distance is elongated to 2.43 Å. Due to the large separation, the E_b at Hol is reduced to -1.41 eV. There are charge transfers from the Pt atoms to PG as these structures show no spin momentum even when the calculations were performed in a spin-polarized way. It should be noted that the estimated amount charge transfer upon deposition is only about 0.10 $|e|$ from the Pt atom to PG. This

suggests the interaction formed between the Pt atom and PG is weak and is accord with the calculated small E_b.

One of the key challenges in fabrication of practical and stable single-atom catalysts is that, single atoms are too mobile and easy to sinter under realistic reaction conditions.[29] The calculated barrier for Pt atoms diffusion from Brg to the nearest neighboring Atop on PG is as low as ~0.14 eV and is in reasonable agreement with previous reports.[53, 54] This low diffusion barrier implies that the deposited Pt atoms are ready to diffuse on PG and will form large particles as the amount of deposited Pt atoms increases. As a result, PG sheet is not eligible as a support material to stabilize the Pt atoms for catalytic applications.

Many studies on supported metal catalysts show that defects of the support materials could serve as anchoring sites for metal clusters and even single atoms. [55-58] There are abundant types of defect on as synthesized graphene. With the help of HR-TEM, the presence of various types of defects in graphene samples has been identified,[59] including clustered pentagons and heptagons, vacancies, edges and contaminations.[60] Theoretically, Wang *et al.* also showed that electron beam irradiation can serve as a useful tool to modify the defect morphology in a controllable manner and to tailor the physical properties of defective graphene.[61] The existence of these defects and their interconversion provide solutions to enhance the TM NP-support interaction and to tune the reactivity of the fabricated composites.[62-64] We investigated the stability of the defects in graphene and found that monovacancies are typical defects and are highly reactive to anchor TM atoms.[64] The fabrication of subnanosized vacancies and stabilization of Pt atoms by the monovacancies over graphene has been realized experimentally.[65, 66] Therefore, monovacancies were considered as the typical defects on graphene.

MG can be generated by removing 1 C atom from PG. To passivate the defect states and stabilize the vacancy, 2 of the three C atoms bond together forming a C_5 ring, while the other C atoms adjacent to the vacancy constitute a C_9 ring. The C-C distance between the 2 newly bonded atoms is shortened from 2.46 Å in the graphene lattice to 2.01 Å, and the remaining C atom with defect states is repelled 0.21 Å out of the basal plane.[67, 68] The calculated formation energy of MG is 7.69 eV[68, 69] and the magnetic momentum is 1.14 μ_B, corresponding to the localized defect states characterized as sharp spikes at the vacant site.[67] Previously, defects like these have also been predicted to alter the electronic properties and modify the chemical reactivity of graphene toward adsorbates.[61, 70-74] In this sense, we expect monovacancies on graphene would act as reactive anchoring point to stabilize the Pt atoms.

Due to the larger size of Pt atoms as compared to C atoms, when a Pt atom is placed at a vacancy on graphene Pt, it moves outward the basal plane of graphene to relax the tension and this outward movement is 1.76 Å. The differential charge density showed that there are significant charge accumulation regions between the Pt atoms and the C atoms and the amount of charge transfer is 0.51 $|e|$ from Pt atom, implying the partially covalent nature of the interaction (Figure 1). The E_b (-7.10 eV) at MG is thus enhanced by more than 2 folds as compared with that on PG. The large E_b of PtMG also makes the outward diffusion of Pt to its neighboring Atop site endothermic by -5.21 eV. The calculated barrier for this diffusion is 5.75 eV and is much higher than the diffusion barrier of ~0.14 eV over PG, which vigorously excludes the clustering of embedded Pt atoms on PtMG. As the fabrication of PtMG has been realized recently, we will focus on PtMG in the following discussion.[36]

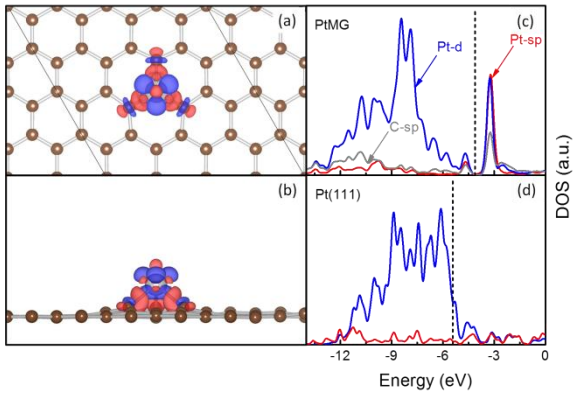

Figure 1. Top view (a) and side view (b) of the contour plot of differential charge density of PtMG, DOS of PtMG (c) and Pt(111) surface (d). (C: Brown; Pt: Silver. The contour value of the differential charge density is ± 0.005 a.u. The charge accumulation regions are in red while the charge depletion regions are in blue. The DOS curves are aligned by the calculated vacuum level which is set as 0 and the E_F of each system is marked with the dashed lines.)

To gain deeper insight into the significantly enhanced E_b in PtMG, the density of states (DOS) curves of the Pt-sp, Pt-d and C-sp states of Pt and C atoms at PtMG are plotted in Figure 1. The DOS of MG with a vacancy is characterized with sharp peaks around the Fermi level (E_F), which is obviously different from the case of PG.[64] After Pt deposition, the sharp spikes corresponding to the localized defect states at the vacancy are shifted downwards and overlap with the Pt-sp and Pt-d states below the E_F, showing the strong hybridization among them. This, together with the differential charge density, suggest that the Pt atom uses its valence states to interact with the defective states of MG. We compared the DOS of PtMG and Pt(111) (Figure 1d) and found that due to the interaction with C atoms at the vacancy, some filled Pt-d states are shifted to the vacuum level and resonance strongly with C-sp states. We also noticed that the E_F of PtMG is higher than that of Pt(111), showing that PtMG has a lower workfunction as compared with Pt(111). The energy levels of localized d states of transition metals are known to be vital for the

activation of adsorbed reactants and subsequent reaction. The existence of the high energy Pt-d states and the lower workfunction originated from the Pt-C interaction, suggest that PtMG may exhibit higher reactivity in activation of adsorbed CO and O_2 for CO oxidation.

3.2 CO, O_2, CO_2 and O adsorption on PtMG

The stability of reactants, intermediates, transition states and products would strongly affect the thermodynamics of a specific reaction. For the CO oxidation over PtMG, the possible reactants and products are O_2, CO, O and CO_2. The structural, electronic and energetic properties of their most plausible adsorption structures are summarized in Table 2 and Figure 2. We noticed that both CO_2 and O_2 are only physisorbed on PG. The adsorption stabilities of CO and O_2 are significantly enhanced on PtMG. The E_{ad}s change from about -0.10 eV to -1.51 and -1.32 eV for CO and O_2, respectively, indicating that both of them can be readily adsorbed onto the PtMG at low temperatures.

Table 2. The E_{ad}s and the most plausible structures of various reaction species adsorption on PtMG.

Species	E_{ad}^{a} (eV)	Bonding Details	
		Bond	Length (Å)
CO	-1.51	C-O	1.16
		Pt-C	1.99
O_2	-1.32	O-O	1.37
		Pt-O	2.15
		Pt-O	2.15
CO_2	-0.07	Pt-O	2.34
		C-O	1.20
		C-O	1.24
O	-4.50	Pt-O	1.82

[a.] The E_{ad} is calculated as the energy difference between the species adsorbed on PtGN and the gaseous species plus the bare PtMG according to equation 2.

CO interacts strongly with the PtMG. The calculated E_{ad} for the most plausible adsorption configuration is -1.51 eV, which is even stronger than the E_{ad} of CO over bulk Pt surfaces(-1.34 eV).[47] In this configuration, CO interacts with the Pt atom with the C-end a little tilted to the basal plane of graphene. Previously, CO tilted adsorption over CuO_x has been observed by Mudiyanselage et al in STM experiments.[75] As the charged Pt and Cu atom are both in d^9 configuration where the John-Teller distortion is significant, they prefer to interaction with CO along the direction of dz^2 state. The C-Pt distance is 1.99 Å, which falls in the range of typical C-Pt chemical bonding. The covalent nature of this interaction is supported by the charge accumulation region between the C and Pt atoms. There is a charge transfer of 0.06 |*e*| from the PtMG to the CO, which is the net result of the donation of CO-5σ electrons to Pt states and the back-donation of Pt-d electrons into the CO-2π* states. This charge transfer activates the CO molecule and this activation is visualized by the charge accumulation region between C and Pt atoms and the charge depletion region between the C and O atoms in the contour plot of differential charge density. Originated from this charge transfer, the C-O distance is elongated from 1.14 Å in a free molecule to 1.16 Å after adsorption. Due to the interaction with the PtMG, all the DOS peaks corresponding to CO states are downshifted and the peak of 2π* orbital is split into parts and even shifted to below E_F. It should be noticed that the variation of the minimum Pt-C distance in PtMG before and after CO adsorption is within 0.03 Å, showing that the CO adsorption will not induce significant structural change of PtMG. Therefore, the previously mentioned contribution of flexibility of TM nanostructures to the catalytic performance[76, 77] may not hold for the case of PtMG.

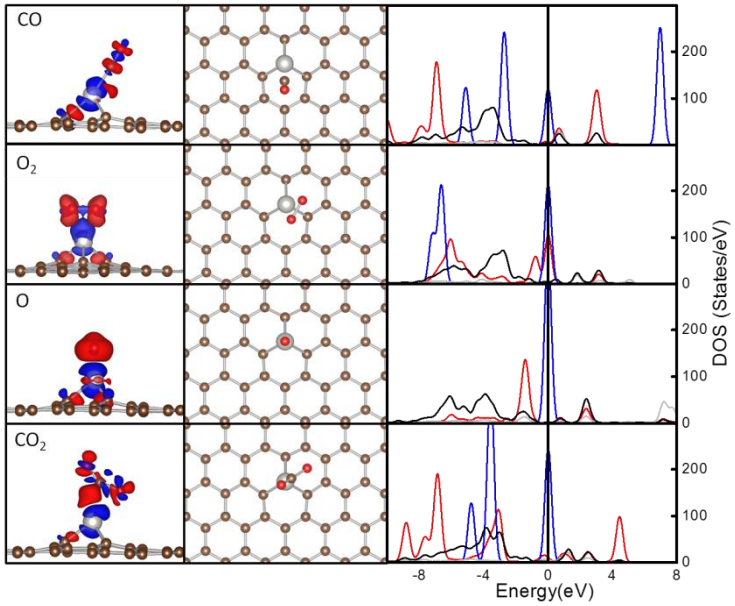

Figure 2. The most plausible adsorption structures (left panel), contour plots of differential charge density (middle panel) and the corresponding DOS curves (right panel) for CO, O_2, O and CO_2 adsorption on PtMG. (C: Brown; Pt: Silver; O: Red. For the contour plots, the charge accumulation regions are rendered in red while the charge deplete regions are shown in blue. The contour value of the differential charge density is ± 0.005 a.u. The DOS curves of free species are in blue and those of absorbed species are in red. The DOS curves of Pt-sp and Pt-d states are in gray and black, respectively. The DOS curves are aligned by the calculated E_F.)

The E_{ad} of O_2 molecule is about 0.2 eV less stable as compared with that of CO and the adsorption configuration is quite different. The O_2 molecule prefers to lie parallel to the basal plane of the graphene, immediately on top of the embedded Pt atom. The 2 nearest Pt-O distances are both 2.15 Å. The amount of charge transfer from Pt to the absorbed O_2 is 0.32 $|e|$. This charge transfer is confirmed by the charge depletion region on the embedded Pt atom and the charge accumulation region on O_2 molecule. After adsorption, the DOS peaks of O_2-5σ and O_2-2π states are downshifted and coincide with those of Pt-d and Pt-sp states (Figures 2),

showing the strong hybridization among them. Furthermore, due to the charge transfer from Pt-d state to the O_2-2π, both the energy level and intensity of O_2-2π state are changed significantly. The elongation of the O-O distance by about 0.2 Å and the charge depletion region between the 2 O atoms vigorously visualize this activation.

We also investigated the O atomic adsorption on PtMG. As compared with the case of O_2, the E_{ad} of O atom is enhanced by about 3.0 eV to -4.50 eV. Similar to the case of O_2 adsorption, the absorbed O atom gains charge from PtMG and the amount of charge transfer is 0.34 |*e*|. The interaction between Pt and O is mainly ionic as visualized by the contour plot of differential charge density. In this sense, the enhancement of O E_{ad} can be understand as the result of removing of repulsive interaction among negative charge absorbed O atoms as compared with the case of O_2. This phenomenon is widely observed in coverage dependent O adsorption on surfaces of transition metals and alloys.[78, 79] In the DOS plots, the peaks of O-sp states overlap with those of Pt-sp and Pt-d states around the E_F, showing the strong hybridization among them. Comparing with peaks of adsorbed O_2, the energy level of O-sp of adsorbed O atom are higher and adjacent to the E_F, which is a sign of the potential high oxidation activity. The shape and distribution of O-sp states of adsorbed O atom are quite similar to those of adsorbed O_2, indicating the effectiveness of PtMG for O_2 activation.

Various possible CO_2 adsorption sites were investigated and the most stable adsorption site locates on the Pt atom with an E_{ad} of -0.07 eV. In this configuration, the Pt atom stands immediately below one of the C-O bond. The nearest O-Pt and C-Pt distances are 2.37 Å and 2.27 Å, respectively, showing the interaction between Pt and CO_2. This interaction is partially covalent as proved by large charge depletion region over Pt and the charge accumulation region between Pt and CO_2, in the Pt-C and Pt-O directions. Due to this interaction, CO_2 is distorted.

One of the C-O distance is elongated to 1.24 Å, the other C-O distance is 1.20 Å and the O-C-O angle is deformed from 180° to 149.18°. Accordingly, the DOS peaks of CO_2 states are downshifted and overlapped with the peaks of Pt-d states. The antibonding states of CO_2 gain charge from the embedded Pt atom and are now crossing the E_F. This, together with the differential charge density, visualize the activation of CO_2 over PtMG, though the adsorption is not stable. Previously, distortion of O-C-O angle at this level was only observed during CO_2 activation and adsorption over framework anions. [80] The CO_2 activation adsorption over PtMG also shows the potential application of PtMG for CO_2 sequestration and conversion.

It should be noted that from an energetic point of view, the adsorption of CO on PtMG is preferred rather than the O_2 molecule. However, the coadsorption of CO and O_2 on the same embedded Pt atom is also an exothermic process and the E_{ad} is even larger than the individual adsorption of O_2. Previously, Kim et al showed that H_2 can take over the absorbed CO at elevated H_2 pressure even though CO binds strongly on subnanosized Pt particles deposited on graphene.[22] Considering the CO catalytic oxidation normally happens in O_2-rich environment or in existence of large amount of H_2, the large free energy change during the reaction process will drive the CO oxidation to proceed over PtMG even though it has a slightly higher affinity to CO.

3.3 CO oxidation over PtMG

In general, CO oxidation can take place through 2 mechanisms, namely the Langmuir-Hinshelwood (LH) and the Eley- Rideal (ER) mechanism, depending on the catalysts involved.[81] The ER mechanism initiates with the direct reaction of gaseous CO molecules with the adsorbed O atom at the reaction centers resulting from the activation of O_2, to form a carbonate-like CO_3 intermediate. The dissociation adsorption of O_2 is the rate-limiting step. This is the common mechanism for CO oxidation over active catalysts that are ready for the dissociation adsorption

of O_2. Different from the ER mechanism, the CO oxidation following LH mechanism starts with the interaction between the coadsorbed CO and O_2 molecules for formation of a peroxide-like O=C-O-O intermediate. As the coadsorbed CO and O_2 are all negatively charged and repulsive to each other, the formation of the peroxide becomes demanding and sets the rate of the process. The reaction of CO with O_2 over PtMG through both the ER and LH mechanisms was investigated.

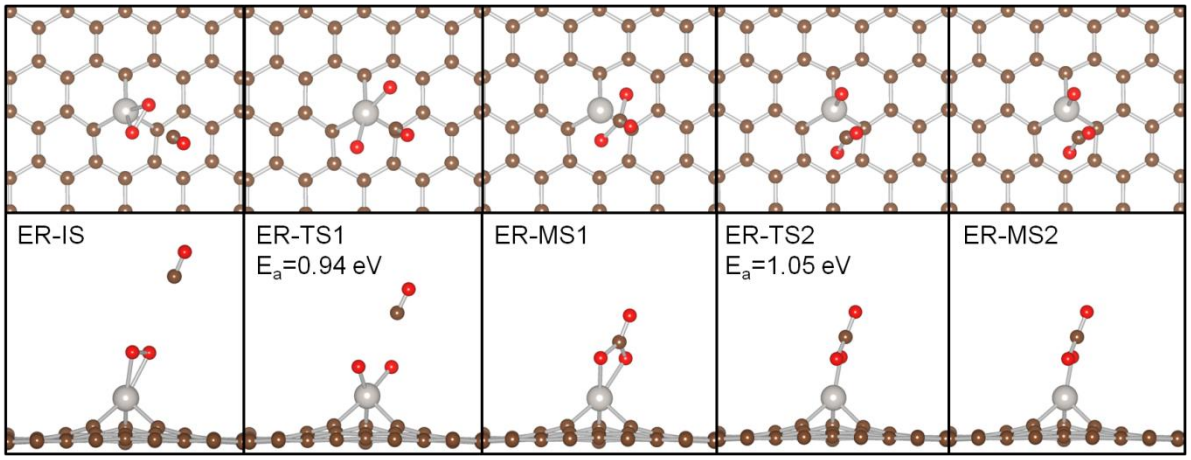

Figure 3. Top views (Top panel) and side views (Bottom panel) of local configurations of the adsorbates on the PtMG at various states along the minimum-energy pathway via the ER mechanism, including the initial state (ER-IS), transition state (ER-TS1 and ER-TS2), intermediate state (ER-MS1) and final state (ER-MS2). (C: Brown; O: Red; Pt: Silver.)

The atomic configurations at various states along the reaction path following the ER mechanism were shown in Figure 3. To search for the minimum-energy path (MEP) for the CO oxidation, the state of gaseous CO and O_2 and clean PtMG was set as the energy zero and the configuration of physisorbed CO above preadsorbed O_2 on the PtMG was selected as the initial state (ER-IS). In ER-IS, the CO lies in plane with the adsorbed O_2 and the distance between the

CO and 2 atoms of the adsorbed O_2 are both 3.63 Å. When the CO molecule approaches the activated O_2, CO is inserted into the O-O bond to form a carbonate-like intermediate state (ER-MS1) on PtMG, where the O-O distance is further elongated to 2.21 Å as compared with 1.37 Å adsorbed O_2. Similar elongation of the O-O distance has been observed in the reaction of CO with O_2 over Fe-embedded graphene and supported Au nanoparticles.[39, 82, 83] This CO insertion is exothermic by 3.20 eV and the corresponding reaction barrier is 0.94 eV (ER-TS1) due to the breaking of the O-O bond and the formation of the new C-O bonds. Then, this reaction MEP connects ER-MS1 with the residual intermediate state (ER-MS2) where the carbonate-like structure in ER-MS1 dissociates by scission of one C-O bond attaching to the Pt atom. This will form a physisorbed CO_2 and an O atom adsorbed on the PtMG. As the ER-MS1 is relatively stable and the adsorbed single O atom is highly reactive, the reaction along this path is endothermic by 0.62 eV with respect to ER-MS1 and requires crossing of another high energy barrier of 1.05 eV(ER-TS2). It should be noted that both the reaction barriers along the MEP starting from ER-IS1 for formation of ER-MS1 and ER-MS2 are more than 0.9 eV, implying that the CO oxidation over PtMG through ER mechanism would be slow due to these high reaction barriers. Furthermore, the coadsorption of CO and O_2 over PtMG (LH-IS1) was found to be 0.83 eV more stable as compared with ER-IS, showing that reaction may initiate on a path different from the ER mechanism. Previously, Lu et al. and Song et al. investigated the CO oxidation over Au and Cu embedded graphene and both of them proposed that LH mechanism is thermodynamically more favorable than the ER mechanism for the CO oxidation to take place.[37, 40] An et al also suggested that CO and O_2 can coadsorbed over helix Au nanotube and the subsequent reaction will proceed through the LH mechanism.[11] Therefore, we moved on to investigate CO oxidation through the LH mechanism.

According to the LH mechanism, the coadsorbed CO and O_2 (LH-IS1) will react to form a peroxide-like intermediate (LH-MS1) and then with the scission of the O-O bond in LH-MS1, a physisorbed CO_2 is formed together with an adsorbed atomic O on the PtMG (LH-MS2). Following this, another gaseous CO molecule will approach to and react with the adsorbed atomic O (LH-IS2) and form a second physisorbed CO_2 (LH-FS). Finally, the catalytic cycle restarts after the desorption of the CO_2 with the coadsorption of O_2 and CO. The most plausible coadsorption structures of CO and O_2, together with the atomic structures at various states along the MEP following the LH mechanism are shown in Figure 4 and Figure 5, with the corresponding structural parameters listed in Table 3 and Table 4.

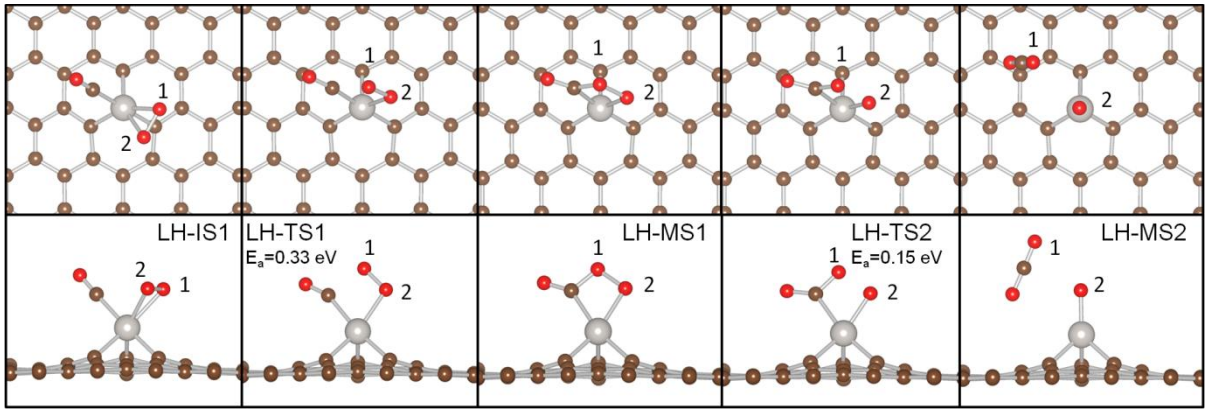

Figure 4. Top views (Top panel) and side views (Bottom panel) of local configurations of the adsorbates on the PtMG at various states along the MEP via the LH mechanism, including the initial state (LH-IS1), transition states (LH-TS1 and LH-TS2), and intermediate states (LH-MS1 and LH-MS2). (C: Brown; O: Red; Pt: Silver.)

Table 3. Structural Parameters for Various States along the MEP for the CO Oxidation over PtMG through LH mechanism.

States	d_{C-O} [a] (Å)	d_{C-Pt} [a] (Å)	d_{C-O1} [a] (Å)	d_{O1-O2} [a] (Å)	d_{O2-Pt} [a] (Å)	$\angle_{O-C-O1}$ [b] (°)
LH-IS1	1.15	2.06	2.94	1.35	2.22	129.6
LH-TS1	1.16	2.13	1.89	1.35	2.17	114.7
LH-MS1	1.21	2.15	1.38	1.47	2.11	120.9
LH-TS2	1.22	2.18	1.31	1.73	2.02	126.3
LH-MS2	1.18	4.09	1.18	3.33	1.83	178.1

[a] The distance between specific atoms. Please see Figure 4 for the nomination of atoms.
[b] The angle among O-C-O1. This angle is 120° in CO_3^{2-} and is 180° in free CO_2.

As CO and O_2 all gains charge from the embedded Pt atom, they are repulsive to each other and this repulsive interaction has a negative contribution of 0.5 eV to the coadsorption. As a result, in LH-IS, the O1-O2 distance decreases slightly to 1.35 Å and the C-Pt distance increases from 1.99 Å to 2.06 Å. Once CO and O_2 are coadsorbed onto the PtMG (LH-IS1), one of the O atom (O1) in the adsorbed O_2 starts to approach the carbon atom of CO to reach the transition state (LH-TS1) that connects LH-IS to LH-MS1. During this endothermic process, the C-O1 distance also decreases from 2.94 Å in LH-IS to 1.89 Å in LH-TS1. Crossing a energy barrier for the formation of LH-MS1 of 0.33 eV, a peroxide-like O2-O1-C-O complex (LH-MS1) is formed. In LH-MS1, the O-O distance is further elongated to 1.47 Å. The O-O distance of this length scale has been only be observed in peroxide before, showing that the LH-MS1 is not stable and the scission of the O-O bond would be facile. As a result, the formation of LH-MS1 is exothermic by 0.30 eV with respect to LH-TS1. Further reaction of LH-MS1 will breaking the O1-O2 bond to form a physisorbed CO_2 and an O atom adsorbed on PtMG (LH-FS1). This process requires passing through an energy barrier of 0.15 eV. At the corresponding transition state (LH-TS2), the O1-O2 distance reaches 1.73 Å, the Pt-C distance is enlarged from 2.13 Å in LH-MS1 to 2.18 Å, while the C-O1 distance is shortened from 1.38 Å to 1.31 Å, implying the

strengthening of the C-O1 interaction and the weakening of the O1-O2 and Pt-C interaction have been initiated. Driven by the strong exothermic formation of the C=O bond in CO_2, LH-MS2 is 2.52 eV more stable as compared with LH-MS1 and the barrier for this reaction step is only 0.15 eV. This suggests that the decomposition of LH-MS1 is a spontaneous process and is ready to take place at low temperatures. As the E_{ad} of CO_2 is only at the level of -0.1 eV, the desorption of CO_2 in LH-MS2 can also be considered to be barrierless. The small reaction barriers and relative high stability of LH-IS1 as compared with ER-IS suggest that the CO oxidation over PtMG would proceed through the LH mechanism rather than the ER mechanism.

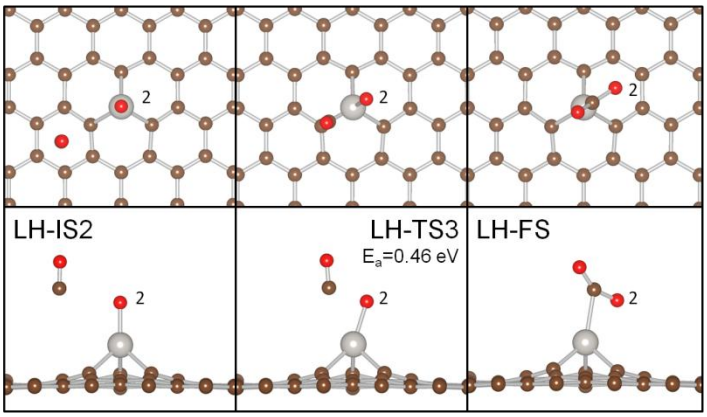

Figure 5. Top views (Top panel) and side views (Bottom panel) of local configurations of the adsorbates on the PtMG at various states along the minimum-energy pathway via the LH mechanism, including the initial state (LH-IS2), transition states(LH-TS3) and final state (LH-FS). (C: Brown; O: Red; Pt: Silver.)

We then investigated the reaction between a gaseous CO molecule and the adsorbed O atom over PtMG. A configuration of the CO molecule stands more than 3.0 Å away from the adsorbed atomic O on PtMG was set as the initial state (LH-IS2, Figure 5). The product was set to the configuration that CO_2 adsorbed on PtMG (LH-FS, Figure 5). In this process, the C atom of CO

approaches to the adsorbed atomic O and pushes it away from the Pt atom to reach the transition state (LH-TS3, Figure 5).

Table 4. Structural Parameters for Various States along the MEP for the CO Oxidation over PtMG through LH mechanism.

States	d_{C-O} [a] (Å)	d_{C-Pt} [a] (Å)	d_{C-O2} [a] (Å)	d_{O2-Pt} [a] (Å)	$\angle_{O-C-O2}$ [b] (°)
LH-IS2	1.14	3.89	3.10	1.82	99.8
LH-TS3	1.16	2.68	1.97	1.93	112.7
LH-FS	1.20	2.27	1.24	2.37	149.2

[a] Distance between specific atoms. Please see Figure 6 for the nomination of atoms.
[b] Angle among O-C-O2. This angle is 120° in CO_3^{2-} and is 180° in CO_2.

Within LH-TS3, the Pt-C distance is decreased from 3.89 Å in LH-IS2 to 2.68 Å and the C-O2 distance is also decreased from 3.10 to 1.97 Å, showing that due to the formation of interaction between CO and O atom, the CO molecule is pushed to the PtMG in this endothermic process. As expected from the high reactivity of the adsorbed O atom and the strong exothermic formation of CO_2, the reaction barrier for formation of LH-FS is 0.46 eV and the reaction is exothermic by 1.63 eV with respect to LH-IS2. The low barrier for formation of LH-FS and the small E_{ad} of CO_2 indicate that the regeneration of PtMG as the available reaction center for subsequent CO oxidation is facile at moderate temperatures. The thermodynamics profile of the MEP for CO oxidation over PtMG is schematically summarized in Figure 6.

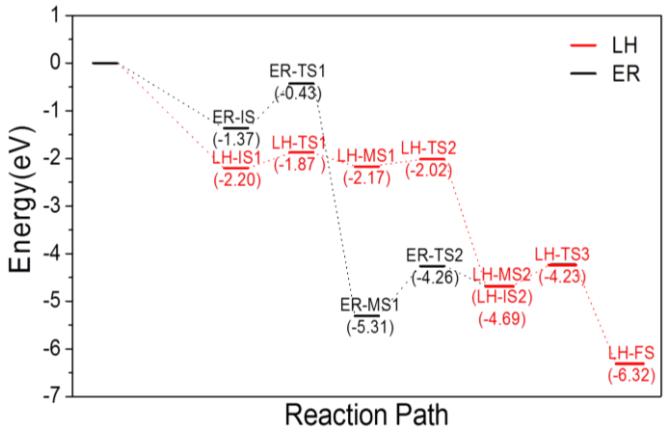

Figure 6. Schematic energy profile corresponding to local configurations shown in Figures 3,4 and 5 along the MEP. All energies are given with respect to the reference energy, i.e., the sum of energies of the clean PtMG and gaseous CO and O_2 molecules.

To gain more insight into the origin of the high activity of PtMG, we investigated the electronic structures of selected atomic configurations through the LH mechanism. Figure 7 shows the projected density of states (PDOS) of CO and O_2 molecular states as well as the Pt-d states in LH-IS1, LH-TS1, LH-MS1, LH-TS2 and LH-MS2, respectively. We investigated the PDOS of every image along the MEP from LH-IS1 to LH-MS2 to trace the evolution of interaction among atoms and assign the composition of each DOS peaks. Due to the minor role of Pt-sp states in CO oxidation, the DOS curves are not shown for clearance. The DOS peaks of Pt-d states, which are crucial for the catalytic activity of PtMG, are standing at right on the E_F due to the interaction between Pt and MG (Figure 1).

Upon CO and O_2 coadsorption, the peaks of Pt-d states are further shifted to crossing the E_F, showing that they are partially occupied in LH-IS1 due to the charge transfer between Pt and adsorbates. The CO-2π* and O_2-2π* states that are of antibonding character, gain electrons and are thus partially filled and downshifted to crossing the E_F. In addition, the peaks of 5σ states of

CO and O_2 are also downshifted to the energy levels of the 1π states and get broadened, which is a sign of the contribution of these states to the coadsorption. In this way, the peaks of O_2-5σ, CO-5σ, CO-1π and O_2-1π overlap in the energy range from -7 eV to the E_F , indicating that interaction is already formed between CO and O_2. The peaks of CO-2π* state and the O_2-2π* state also coincide in the range from -1 eV to 1 eV, which implies the interaction between CO and O_2 is weak in LH-IS1.

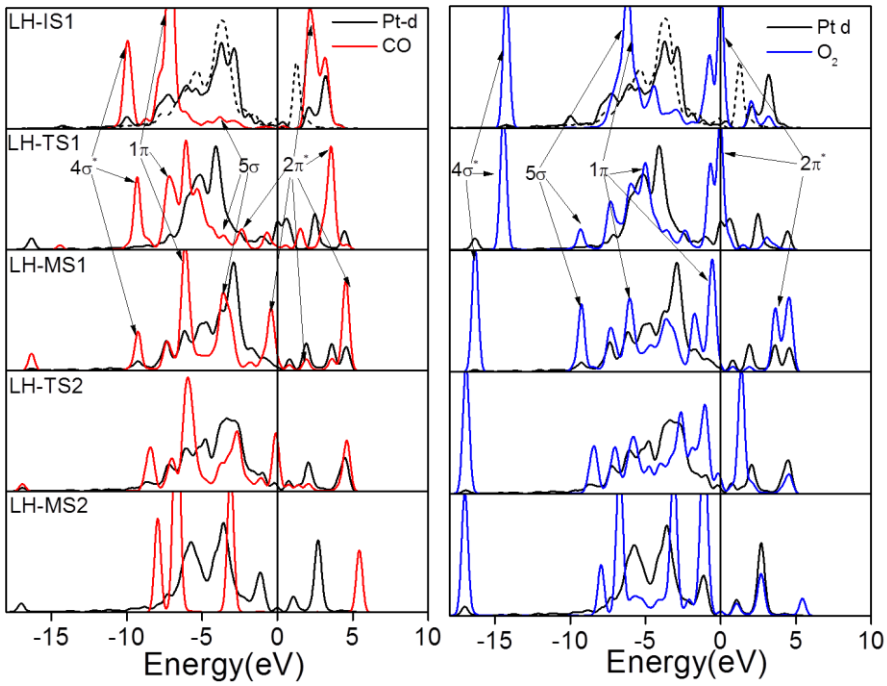

Figure 7. PDOS of CO(left panel),O_2 (right panel) and Pt atom in the LH-IS1, LH-TS1, LH-MS1, LH-TS2 and LH-MS2. The DOS plots were aligned by the calculated Fermi level. The DOS of clean PtMG was shown as short-dashed lines.

From LH-IS1 to LH-TS1, the DOS peaks of O_2-1π, O_2-5σ and O_2-2π* states are further downshifted, broadened and overlap with those of CO molecular states, as the result of the evolution of interaction between the coadsorbed molecules. In LH-TS1, as the C-O1 interaction

are getting mature, the DOS peaks of O_2 states resonance strongly with those of CO states in the range from -10 eV below E_F to 2 eV above E_F. The peak of O_2 state even overlaps with the CO-4σ state, showing that the C-O interaction in CO is significantly weakened and new C-O1 interaction is formed. But these C-O interactions are weak as the resonance between O_2-2π* and CO-2π* of antibonding nature are still strong in the range from -1.5 eV to 1.5 eV. However, the resonance between the CO and O_2 molecular states and Pt-d states of bonding nature is weakened as compared with that in LH-IS1 at about -5 eV, which provides direct evidence for the interaction between Pt and adsorbed molecules, the unstability of LH-TS1 and the tendency for formation of the peroxide-like intermediate (LH-MS1).

Compared with the DOS plot of LH-TS1, the peaks of adsorbates are narrowed in LH-MS1. The DOS peak at -15 eV, originated from the O_2-4σ state is downshifted and overlaps with the CO states, showing that the C-O1 interaction is further strengthened. The intensity of peaks of O_2 states is enhanced in the range from -10 eV to E_F, proving that O_2 is activated and C-O1 bonding is stabilized. This is also evidenced by the strong resonance between CO and O_2 states in this energy range. The large broad resonance peak in the range from -7.5 eV to -4.0 eV is split into 2 parts. The part below -5 eV corresponds to the enhanced C-O1 interaction, while the part above -5 eV corresponds to the C-Pt and O2-Pt interactions. These occupied states are of bonding nature and contribute to the stability of the peroxide-like intermediate on the embedded Pt atom. The reduced intensity of peaks of partial occupied CO and O_2 antibonding states, which are standing on the E_F and resonance with the Pt-d states, shows that this peroxide-like intermediate is ready to dissociate by scission of the O1-O2, C-Pt and O-Pt bonds with the involvement of the Pt-d states.

The DOS peaks of the O_2 and CO states standing at the E_F are split into 2 parts, when the structure evolves from LH-MS1 to LH-TS2. The part that corresponds to the antibonding interaction between C and O1 is shifted upward and hybrids with the Pt-d states, which is a sign of further enhancement of the C-O1 interaction. The part corresponds to the bonding interaction between C-Cu and O1-Pt is downshifted. This synchronizes the formation and desorption of CO_2 over PtMG. During the whole process, the hybridization between the Pt-d states and molecular states of CO and O_2, proving the significant catalytic role of Pt-d states in coadsorption and subsequent reactions.

In summary, the CO oxidation over PtMG may be characterized as a two-step process: The CO catalytic oxidation cycle is initiated through the LH mechanism, where the coadsorbed CO and O_2 (LH-IS1) react to form a peroxide like complex (LH-MS1), by the dissociation of which the a CO_2 molecule and an adsorbed O atom are formed (LH-MS2), and then the PtMG is regenerated to be available by the reaction of a gaseous CO with the adsorbed O atom (LH-IS2) to form another CO_2 (LH-FS). The potential high performance of PtMG can be attributed to the compatibility of the states of PtMG and adsorbed intermediates, particularly among the Pt-d states and the molecular states of CO and O_2, that facilitates the required charge transfer for the reaction to proceed.[11]

4. CONCLUSIONS

We investigated the electronic structure of Pt atoms embedded in defective graphene and their catalytic role in CO oxidation by first-principles based calculations. We showed that the combination of highly reactivity Pt atoms and defects over graphene makes the Pt embedded graphene a superior mono-dispersed atomic catalysts for CO oxidation. The binding of a single Pt atom onto single vacancy defects is up to -7.0 eV which not only ensure the high stability of

the embedding, but also vigorously excludes the diffusion and aggregation of embedded Pt atoms. The strong binding of Pt atoms also up-shifts the energy level of Pt-d states and promote the reactivity, so that the activation of the adsorbed O_2 and formation of peroxide-like intermediate becomes facile. The catalytic cycle of CO oxidation is initiated through the Langmuir–Hinshelwood mechanism, where the coadsorbed CO and O_2 react to form a peroxide-like complex, by the dissociation of which the a CO_2 molecule and an adsorbed O atom are formed. Then, the embedded Pt atom is regenerated by the reaction of another gaseous CO with the remnant O atom. The calculated energy barriers for the formation and dissociation of peroxide-like intermediate are as low as 0.33 and 0.15 eV, respectively, while that for the regeneration of the embedded Pt atom is only 0.46 eV, indicating the potential high catalytic performance of Pt-embedded graphene for low temperature CO oxidation.

ACKNOWLEDGMENT

This work was supported by NSFC (21373036, 21103015, 21271037 and 11174045), the Fundamental Research Funds for the Central Universities (DUT14LK09 and DUT12LK14), the Key Laboratory of Coastal Zone Environmental Processes YICCAS (201203), the Key Science and Technology International Co-operation Foundation of Hainan Province, China (KJHZ2014-08) and the Special Academic Partner GCR Program from King Abdullah University of Science and Technology. Y. H would also thank Dalian University of Technology for the Seasky Professorship.

REFERENCES

1. C. J. Zhang and P. Hu, *J. Am. Chem. Soc.*, 2001, **123**, 1166-1172.
2. A. Alavi, P. J. Hu, T. Deutsch, P. L. Silvestrelli and J. Hutter, *Phys. Rev. Lett.*, 1998, **80**, 3650-3653.
3. A. Eichler, *Surf. Sci.*, 2002, **498**, 314-320.

4. A. Eichler and J. Hafner, *Phys. Rev. B*, 1999, **59**, 5960-5967.
5. Z.-P. Liu and P. Hu, *J. Chem. Phys.*, 2001, **115**, 4977-4980.
6. S.-H. Oh and G. B. Hoflund, *J. Catal.*, 2007, **245**, 35-44.
7. Q. Fu, W. X. Li, Y. X. Yao, H. Y. Liu, H. Y. Su, D. Ma, X. K. Gu, L. M. Chen, Z. Wang, H. Zhang, B. Wang and X. H. Bao, *Science*, 2010, **328**, 1141-1144.
8. B. T. Qiao, A. Q. Wang, X. F. Yang, L. F. Allard, Z. Jiang, Y. T. Cui, J. Y. Liu, J. Li and T. Zhang, *Nat. Chem.*, 2011, **3**, 634-641.
9. J. Lin, B. T. Qiao, J. Y. Liu, Y. Q. Huang, A. Q. Wang, L. Li, W. S. Zhang, L. F. Allard, X. D. Wang and T. Zhang, *Angewandte Chemie-International Edition*, 2012, **51**, 2920-2924.
10. J.-X. Liu, H.-Y. Su, D.-P. Sun, B.-Y. Zhang and W.-X. Li, *J. Am. Chem. Soc.*, 2013, **135**, 16284-16287.
11. W. An, Y. Pei and X. C. Zeng, *Nano Lett.*, 2008, **8**, 195-202.
12. A. A. Herzing, C. J. Kiely, A. F. Carley, P. Landon and G. J. Hutchings, *Science*, 2008, **321**, 1331-1335.
13. S. Vajda, M. J. Pellin, J. P. Greeley, C. L. Marshall, L. A. Curtiss, G. A. Ballentine, J. W. Elam, S. Catillon-Mucherie, P. C. Redfern, F. Mehmood and P. Zapol, *Nat. Mater.*, 2009, **8**, 213-216.
14. Y. Lei, F. Mehmood, S. Lee, J. Greeley, B. Lee, S. Seifert, R. E. Winans, J. W. Elam, R. J. Meyer, P. C. Redfern, D. Teschner, R. Schlogl, M. J. Pellin, L. A. Curtiss and S. Vajda, *Science*, 2010, **328**, 224-228.
15. X. Zhang, H. Shi and B. Q. Xu, *Angew. Chem.-Int. Edit.*, 2005, **44**, 7132-7135.
16. X. Liu, S. B. Zhang, X. C. Ma, J. F. Jia, Q. K. Xue, X. H. Bao and W. X. Li, *Appl. Phys. Lett.*, 2008, **93**, 093105.
17. B. Hammer and J. K. Norskov, in *Advances in Catalysis*, Academic Press Inc, San Diego, 2000, pp. 71-129.
18. I. N. Remediakis, N. Lopez and J. K. Norskov, *Angew. Chem.-Int. Edit.*, 2005, **44**, 1824-1826.
19. L. Li, A. H. Larsen, N. A. Romero, V. A. Morozov, C. Glinsvad, F. Abild-Pedersen, J. Greeley, K. W. Jacobsen and J. K. Norskov, *J. Phys. Chem. Lett.*, 2013, **4**, 222-226.
20. J. Oh, T. Kondo, D. Hatake, K. Arakawa, T. Suzuki, D. Sekiba and J. Nakamura, *J. Phys. Chem. C*, 2012, **116**, 7741-7747.
21. J. Oh, T. Kondo, D. Hatake, Y. Iwasaki, Y. Honma, Y. Suda, D. Sekiba, H. Kudo and J. Nakamura, *J. Phys. Chem. Lett.*, 2010, **1**, 463-466.
22. G. Kim and S.-H. Jhi, *ACS Nano*, 2011, **5**, 805-810.
23. M. S. Chen and D. W. Goodman, *Chem. Soc. Rev.*, 2008, **37**, 1860-1870.
24. Y. X. Yao, X. Liu, Q. Fu, W. X. Li, D. L. Tan and X. H. Bao, *ChemPhysChem*, 2008, **9**, 975-979.
25. M. Bowker, *Nat. Mater.*, 2002, **1**, 205-206.
26. J. Zhang, X. Liu, M. N. Hedhili, Y. Zhu and Y. Han, *ChemCatChem*, 2011, **3**, 1294-1298.
27. W. Gao, J. E. Mueller, J. Anton, Q. Jiang and T. Jacob, *Angew. Chem.-Int. Edit.*, 2013, **52**, 14237-14241.
28. A. Corma, P. Concepcion, M. Boronat, M. J. Sabater, J. Navas, M. J. Yacaman, E. Larios, A. Posadas, M. A. Lopez-Quintela, D. Buceta, E. Mendoza, G. Guilera and A. Mayoral, *Nat. Chem.*, 2013, **5**, 775-781.
29. A. Uzun, V. Ortalan, N. D. Browning and B. C. Gates, *J. Catal.*, 2010, **269**, 318-328.

30. A. V. Krasheninnikov, P. O. Lehtinen, A. S. Foster, P. Pyykko and R. M. Nieminen, *Phys. Rev. Lett.*, 2009, **102**, 126807.
31. X. Liu, C. G. Meng and Y. Han, *J. Phys. Chem. C*, 2013, **117**, 1350-1357.
32. X. Liu, C. G. Meng and Y. Han, *Nanoscale*, 2012, **4**, 2288-2295.
33. X. Liu, L. Li, C. G. Meng and Y. Han, *J. Phys. Chem. C*, 2012, **116**, 2710-2719.
34. K. X. Yao, X. Liu, Z. Li, C. C. Li, H. C. Zeng and Y. Han, *ChemCatChem*, 2012, **4**, 1938-1942.
35. X. Liu, C. Meng and Y. Han, *Phys. Chem. Chem. Phys.*, 2012, **14**, 15036-15045.
36. H. Wang, Q. Wang, Y. Cheng, K. Li, Y. Yao, Q. Zhang, C. Dong, P. Wang, U. Schwingenschlögl, W. Yang and X. X. Zhang, *Nano Lett.*, 2011, **12**, 141-144.
37. Y. H. Lu, M. Zhou, C. Zhang and Y. P. Feng, *J. Phys. Chem. C*, 2009, **113**, 20156-20160.
38. F. Li, J. Zhao and Z. Chen, *J. Phys. Chem. C*, 2011, **116**, 2507–2514.
39. Y. Li, Z. Zhou, G. Yu, W. Chen and Z. Chen, *J. Phys. Chem. C*, 2010, **114**, 6250-6254.
40. E. H. Song, Z. Wen and Q. Jiang, *J. Phys. Chem. C*, 2011, **115**, 3678-3683.
41. B. Delley, *J. Chem. Phys.*, 1990, **92**, 508-517.
42. B. Delley, *J. Chem. Phys.*, 2000, **113**, 7756-7764.
43. J. P. Perdew, K. Burke and M. Ernzerhof, *Phys. Rev. Lett.*, 1996, **77**, 3865-3868.
44. B. Delley, *Phys. Rev. B*, 2002, **66**, 155125.
45. X. Liu, C. G. Meng and C. H. Liu, *Phase Transit.*, 2006, **79**, 249-259.
46. X. Liu, C. G. Meng and C. H. Liu, *Acta Phys.-Chim. Sin.*, 2004, **20**, 280-284.
47. M. Gajdos, A. Eichler and J. Hafner, *J. Phys.-Condes. Matter*, 2004, **16**, 1141-1164.
48. A. H. Castro Neto, F. Guinea, N. M. R. Peres, K. S. Novoselov and A. K. Geim, *Rev Mod Phys*, 2009, **81**, 109-162.
49. H. J. Monkhorst and J. D. Pack, *Phys. Rev. B*, 1976, **13**, 5188-5192.
50. F. L. Hirshfeld, *Theor. Chim. Acta*, 1977, **44**, 129-138.
51. N. Govind, M. Petersen, G. Fitzgerald, D. King-Smith and J. Andzelm, *Comput. Mater. Sci.*, 2003, **28**, 250-258.
52. H. Sun, H. Guo, W. Wu, X. Liu and J. Zhao, *Dalton Trans.*, 2011, **40**, 7834-7841.
53. K.-j. Kong, Y. Choi, B.-H. Ryu, J.-O. Lee and H. Chang, *Materials Science and Engineering: C*, 2006, **26**, 1207-1210.
54. P. Blonski and J. Hafner, *J. Chem. Phys.*, 2011, **134**.
55. M. S. Chen and D. W. Goodman, *Science*, 2004, **306**, 252-255.
56. D. Matthey, J. G. Wang, S. Wendt, J. Matthiesen, R. Schaub, E. Laegsgaard, B. Hammer and F. Besenbacher, *Science*, 2007, **315**, 1692-1696.
57. J. H. Kwak, J. Z. Hu, D. Mei, C. W. Yi, D. H. Kim, C. H. F. Peden, L. F. Allard and J. Szanyi, *Science*, 2009, **325**, 1670-1673.
58. S. Sun, G. Zhang, N. Gauquelin, N. Chen, J. Zhou, S. Yang, W. Chen, X. Meng, D. Geng, M. N. Banis, R. Li, S. Ye, S. Knights, G. A. Botton, T.-K. Sham and X. Sun, *Sci. Rep.*, 2013, **3**, 1775.
59. W. S. Hummers and R. E. Offeman, *J. Am. Chem. Soc.*, 1958, **80**, 1339-1340
60. C. Gomez-Navarro, J. C. Meyer, R. S. Sundaram, A. Chuvilin, S. Kurasch, M. Burghard, K. Kern and U. Kaiser, *Nano Lett.*, 2010, **10**, 1144-1148.
61. Z. Wang, Y. G. Zhou, J. Bang, M. P. Prange, S. B. Zhang and F. Gao, *J. Phys. Chem. C*, 2012, **116**, 16070-16079.
62. F. Banhart, J. Kotakoski and A. V. Krasheninnikov, *ACS Nano*, 2010, **5**, 26-41.
63. A. Hashimoto, K. Suenaga, A. Gloter, K. Urita and S. Iijima, *Nature*, 2004, **430**, 870-873.

64. X. Liu, Y. Sui, C. Meng and Y. Han, *RSC Adv.*, 2014, **4**, 22230-22240.
65. Y. Yamada, K. Murota, R. Fujita, J. Kim, A. Watanabe, M. Nakamura, S. Sato, K. Hata, P. Ercius, J. Ciston, C. Y. Song, K. Kim, W. Regan, W. Gannett and A. Zettl, *J. Am. Chem. Soc.*, 2014, **136**, 2232-2235.
66. H. T. Wang, Q. X. Wang, Y. C. Cheng, K. Li, Y. B. Yao, Q. Zhang, C. Z. Dong, P. Wang, U. Schwingenschlogl, W. Yang and X. X. Zhang, *Nano Lett.*, 2012, **12**, 141-144.
67. O. V. Yazyev and L. Helm, *Phys. Rev. B*, 2007, **75**, 125408.
68. Y. Ma, P. O. Lehtinen, A. S. Foster and R. M. Nieminen, *New J. Phys.*, 2004, **6**, 68.
69. P. A. Thrower and R. M. Mayer, *Phys. Status Solidi A*, 1978, **47**, 11-37.
70. J. Kotakoski, A. V. Krasheninnikov, U. Kaiser and J. C. Meyer, *Phys. Rev. Lett.*, 2011, **106**, 105505.
71. J. M. Carlsson and M. Scheffler, *Phys. Rev. Lett.*, 2006, **96**, 046806.
72. D. W. Boukhvalov and M. I. Katsnelson, *Nano Lett.*, 2008, **8**, 4373-4379.
73. D. Ghosh, G. Periyasamy and S. K. Pati, *J. Phys. Chem. C*, 2013, **117**, 21700-21705.
74. P. A. Denis and F. Iribarne, *J. Phys. Chem. C*, 2013, **117**, 19048-19055.
75. K. Mudiyanselage, W. An, F. Yang, P. Liu and D. J. Stacchiola, *Phys. Chem. Chem. Phys.*, 2013, **15**, 10726-10731.
76. W. An and P. Liu, *J. Phys. Chem. C*, 2013, **117**, 16144-16149.
77. W. An, E. A. Baber, F. Xu, M. Soldemo, J. Weissenrieder, D. Stacchiola and P. Liu, *ChemCatChem*, 2014, **In Press**, DOI: 10.1002/cctc.201402177.
78. W. X. Li, C. Stampfl and M. Scheffler, *Phys. Rev. B*, 2002, **65**, 075407.
79. X. Liu, H. Guo and C. Meng, *J. Phys. Chem. C*, 2012, **116**, 21771-21779.
80. Y. Zhao, X. Liu, K. X. Yao, L. Zhao and Y. Han, *Chem. Mat.*, 2012, **24**, 4725-4734.
81. K. J. Laidler, *Pure Appl. Chem.*, 1996, **68**, 149-192.
82. C. Liu, Y. Tan, S. Lin, H. Li, X. Wu, L. Li, Y. Pei and X. C. Zeng, *J. Am. Chem. Soc.*, 2013, **135**, 2583-2595.
83. Z.-P. Liu, P. Hu and A. Alavi, *J. Am. Chem. Soc.*, 2002, **124**, 14770-14779.